LASER INTERFEROMETER GRAVITATIONAL WAVE OBSERVATORY
- LIGO -
CALIFORNIA INSTITUTE OF TECHNOLOGY
MASSACHUSETTS INSTITUTE OF TECHNOLOGY

Technical Note	**LIGO-T2400239–v1**	2024/10/04

Characterization and Modeling of the LLO Squeezing System

David Smith

California Institute of Technology
LIGO Project, MS 18-34
Pasadena, CA 91125
Phone (626) 395-2129
Fax (626) 304-9834
E-mail: info@ligo.caltech.edu

Massachusetts Institute of Technology
LIGO Project, Room NW22-295
Cambridge, MA 02139
Phone (617) 253-4824
Fax (617) 253-7014
E-mail: info@ligo.mit.edu

LIGO Hanford Observatory
Route 10, Mile Marker 2
Richland, WA 99352
Phone (509) 372-8106
Fax (509) 372-8137
E-mail: info@ligo.caltech.edu

LIGO Livingston Observatory
19100 LIGO Lane
Livingston, LA 70754
Phone (225) 686-3100
Fax (225) 686-7189
E-mail: info@ligo.caltech.edu

http://www.ligo.caltech.edu/

Introduction

The introduction of frequency dependent quantum squeezing during the A+ upgrade has allowed both the Hanford and Livingston LIGO observatories to operate below the standard quantum limit. The injection of a squeezed vacuum into the dark port of the interferometer allows one of the two conjugate properties of light, phase or amplitude, to be 'squeezed', increasing the certainty in one property at the cost of increased uncertainty in the other. A 300m optical filter cavity is used to rotate the squeezed quadrature to amplitude squeezing at low frequencies, which reduces quantum radiation pressure noise, keeping the phase squeezing at high frequencies in order to reduce shot noise. While the quantum squeezing system has shown remarkable results in increasing the binary neutron star (BNS) range for both the H1 and L1 detectors, striving for higher squeezing levels is an uphill battle against the many sources of loss that degrade the squeezed vacuum. Factors such as phase noise, optical loss, and mode mismatch limit the injected squeezing, while parameters such as cavity detuning and laser power build up within the interferometer arms affect the frequency dependent effects of squeezing. Having an up-to-date knowledge of the current sources of loss and how they change in response to commissioning changes is crucial in guiding optimal squeezer operation and future detector upgrades. In this paper, we first build and test methods for squeezing characterization, then perform a deeper analysis on mode mismatch loss through the construction of an optical model of the squeezed vacuum path, towards a complete physical model.

Part One: Squeezer Characterization

Current methods of characterization focus on matching quantum noise models generated using the Gravitational Wave Interferometer Noise Calculator (GWINC) to quantum noise spectra taken from the interferometer. However, with more than 25 free parameters, fitting quantum noise models to interferometer data is challenging. Previous work has shown that Markov chain Monte Carlo (MCMC) simulations can be used to successfully infer key interferometer parameters, yet these simulations are often computationally slow and require relatively accurate starting guesses among other parameters [1]. An alternative strategy first used at LIGO Hanford Observatory is the use of the Interactive Squeeze program which allows users to hand fit quantum noise models using an interactive interface, resulting in quicker, yet less accurate results [2]. We will first adapt and expand this interactive fitting code to allow for analysis and comparison of multiple different DARM data sets before testing the hand-fitted results against a modified MCMC algorithm to better understand the parameter space.

Quantum Noise Modeling

GWINC modeling allows for the calculation of quantum noise budgets based on a set of interferometer parameters. While there are a wide array of detector parameters that effect the quantum noise curve, the parameters that are the most important and will be the focus of study are:

- Squeezing angle
- Arm Power
- Phase Noise
- Filter Cavity Detuning
- Injected Squeezing
- Injection Loss
- Signal Extraction Cavity (SEC) Detuning
- Filter Cavity Mismatch
- Filter Cavity Mismatch Phase
- IFO-OMC Mismatch
- IFO-OMC Mismatch Phase
- SQZ-OMC Mismatch
- SQZ-OMC Mismatch Phase

While some parameters such as SEC detuning and arm power can be estimated using independent measurements, others, such as the mode mismatches, are more difficult to directly measure. Using GWINC, we can infer these parameters by fitting models to DARM spectra. However, since DARM data is influenced by both classical and quantum noise sources, in order to compare to GWINC models, the quantum noise needs to be isolated. While there are multiple methods of doing this such as inferring classical noise from the cross-correlation [3] or modeling darm difference [1], the most straight forward method which we will implement is the subtraction of an unsqueezed quantum noise model. Using data taken without squeezing, the classical noise can be inferred by subtracting an unsqueezed quantum noise model from the unsqueezed interferometer data. Since the unsqueezed quantum noise model is independent of the squeezing parameters, this model can be generated with only a few assumptions about the interferometer parameters. Further, as seen in Fig. 1, many of these parameters have negligible impact on the quantum noise curve, allowing them to still be used as free parameters in our model, provided their values don't change drastically from an initial guess. In the case of arm power, previous analysis has narrowed the value down to 308 kW which we will use for our analysis [4]. Using the measured reference no squeezing power spectral density (PSD), R_{psd}, and modeled no squeezing quantum noise PSD, M_{psd}, we can calculate the quantum noise PSD of any squeezed data, D_{psd}, by subtraction of the inferred classical noise [5]:

$$Q_{psd} = D_{psd} - (R_{psd} - M_{psd})$$

Figure 2 shows this subtraction realized.

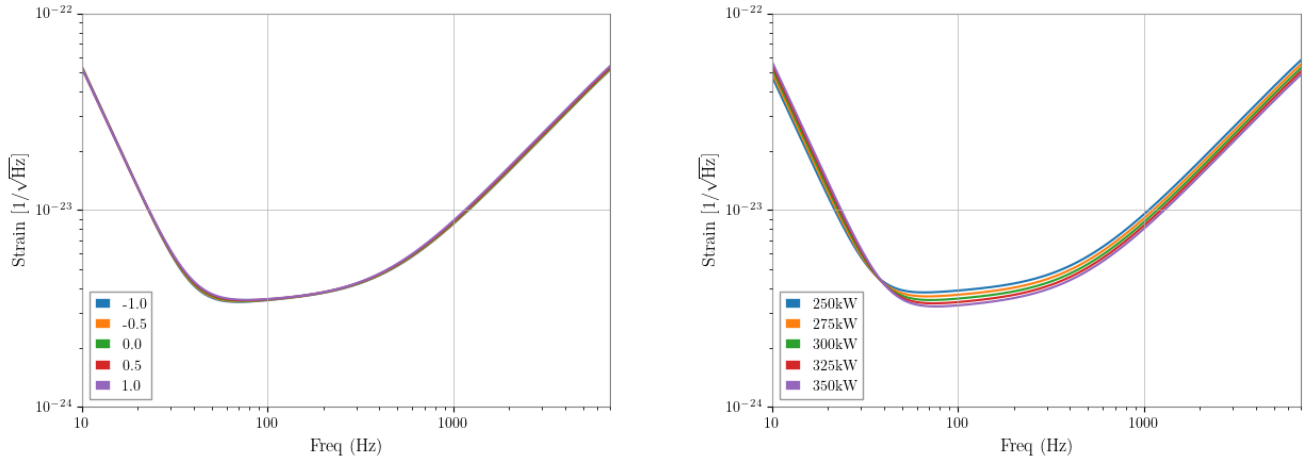

((a)) SEC Detuning ((b)) Arm Power

Figure 1: Unsqueezed quantum noise models for five different values of SEC detuning (a) and arm power (b). SEC detuning has little effect on the quantum noise model over the range -1 to 1. Arm power has a more noticeable effect on the unsqueezed model which constrains its range as a free parameter in order to maintain an accurate classical noise subtraction.

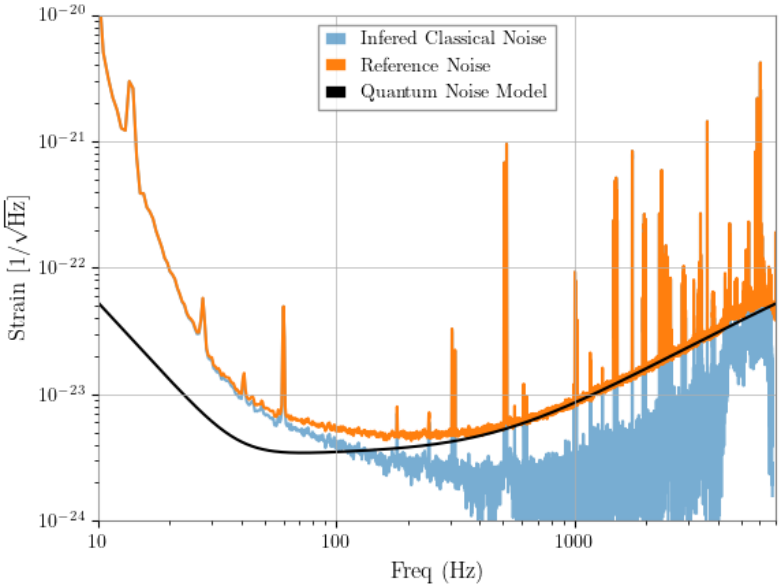

Figure 2: Classical noise (blue) is inferred by subtracting a no squeezing quantum noise model (black) from no squeezing DARM data (orange).

Interactive Parameter Fitting

While methods such as regression fitting and MCMC fitting have been used in the past to fit quantum noise models to DARM data [1], we will start by analyzing data using a hand-fitting interface. Ideally, this method should provide a quicker and more intuitive method

to infer interferometer parameters than MCMC modeling. To achieve accurate fits, both frequency dependent and frequency independent data taken at multiple different squeezing angles is needed to better constrain the parameters. The program pulls data from the L1:GDS-CALIB_STRAIN_NOLINES channel using provided GPS start times and measurement durations. The power spectral density for each squeezing angle is then computed before the inferred classical noise is subtracted. Quantum noise models for each angle are generated using the set of initial parameters and plotted over the DARM spectra. Twelve sliders are then used to dynamically change the parameters listed above in order to match the quantum noise models to the spectra. All other interferometer parameters are set using a noise budget generated on data taken on October 23, 2023 [6], since we do not expect change in parameters such as SRM (signal recycling mirror) transmission. Each squeezing angle's fit is quantified by the root-mean square error, defined as

$$RMSE = \sqrt{\frac{1}{N}\sum_{i=0}^{N}(Q_i - M_i)^2}$$

where x_i is the subtracted DARM spectra and $\hat{x}_i$ is the quantum noise model. The error is calculated separately in five different frequency bands: 20 Hz to 100 Hz, 40 Hz to 100 Hz, 100 Hz to 1000 Hz, 1000 Hz to 3000 Hz, and 3000 Hz to 6000 Hz. The error then is displayed as a bar-chart that dynamically updates as the parameters change, providing an additional visual indicator of the fit. Although the core code remains the same, we have made some additions to the peripheral code based on our needs [7]. One of the main features added to the code is the ability to connect multiple instances of the program together. Parameters can be 'linked' between models, allowing for comparison between data taken at multiple different times. For instance, frequency dependent data can be linked to frequency independent data. Parameters expected to be constant between the two measurements can be linked, while other parameters can be independently varied. The data can either be plotted with the y-axis as regular strain in units of $\frac{1}{\sqrt{Hz}}$, or in decibels relative to the unsqueezed quantum noise model. This method is usually preferred since squeezing level is more intuitively understood in decibels.

The process of fitting the quantum noise models to DARM spectra is deceptively tricky due to degeneracy between parameters. For instance, varying IFO-OMC mismatch phase and SQZ-OMC mismatch phase together leaves quantum noise models relatively unchanged as seen in Fig. 3. Similarly, changes in injected squeezing can be compensated with changes in the squeezing angles. This degeneracy can be somewhat constrained using the fact that the squeezing measurement is ideally taken at the squeezing angle that minimizes the shot-noise around 2000 Hz. Contrarily, the antisqueezing measurement is taken at the squeezing angle that maximizes shot noise. This adds the additional constraint that an accurate fit must have a maximized squeezing and anti-squeezing angle. Maximizing the squeezing angle helps resolve the degeneracy between the mode mismatch phases while maximizing anti-squeezing helps fit an accurate value for the injected squeezing.

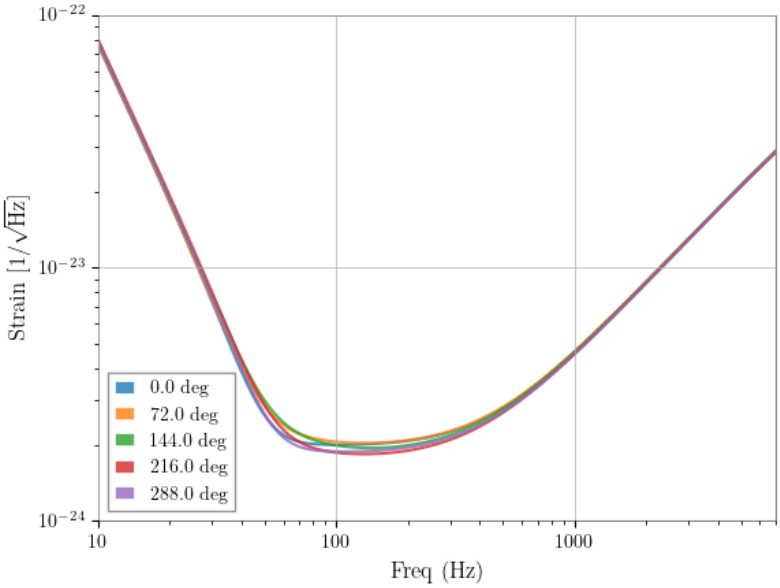

Figure 3: Five squeezing quantum noise models with IFO-OMC mismatch phase and SQZ-OMC mismatch phase varied together through five different angles. The curve remains relatively fixed except for small deviations in the mid frequency range. With the uncertainty present in actual DARM data, these small deviations are hard to catch, leading to possible false fits.

Hand-Fitted Results

Frequency dependent data was taken on March 19th 2024 at six different squeezing angles [8]. Frequency independent data was taken on April 9th 2024 at another six squeezing angles. The start time in GPS and duration for each of the used DARM spectra is listed in Tables 1 and 2, respectively. The frequency independent data was fitted first, then linked to the frequency dependent data in order to fit the filter cavity parameters. The fitted plots and the root-mean squared error for each is shown in Fig. 4 and Fig. 5.

The fits for the frequency independent data are quite good with most fits having a RMSE

Measurement	GPS Time	Duration (s)
Mar. 19 No Sqz	1394847926	500
FDS	1394848796	2000
FDAS	1394847387	400
FD angle 1	1394844446	600
FD angle 2	1394845956	600
FD angle 3	1394846761	300
FD angle 4	1394844058	300

Table 1: Frequency dependent measurement time and duration

Measurement	GPS Time	Duration (s)
Apr. 9 No Sqz	1396733044	590
FIS	1396733821	414
FIAS	1396734551	467
FI angle 1	1396735202	411
FI angle 2	1396735747	486
FI angle 3	1396736351	480
FI angle 4	1396737003	464

Table 2: Frequency independent measurement time and duration

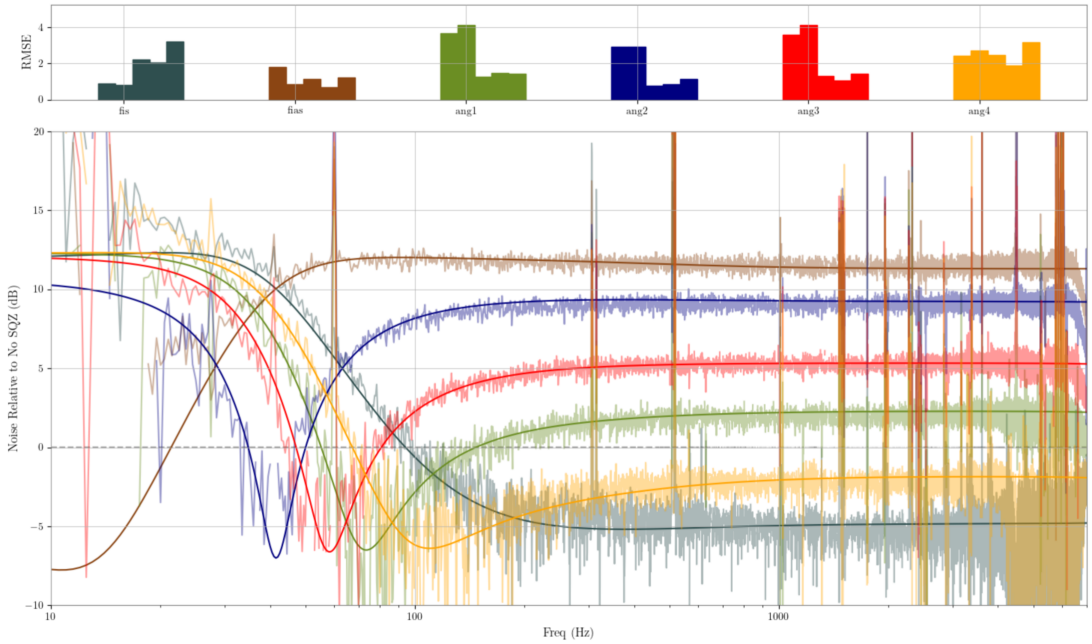

Figure 4: Frequency Independent fits with the RMSE for each fit and frequency range plotted above as a bar chart.

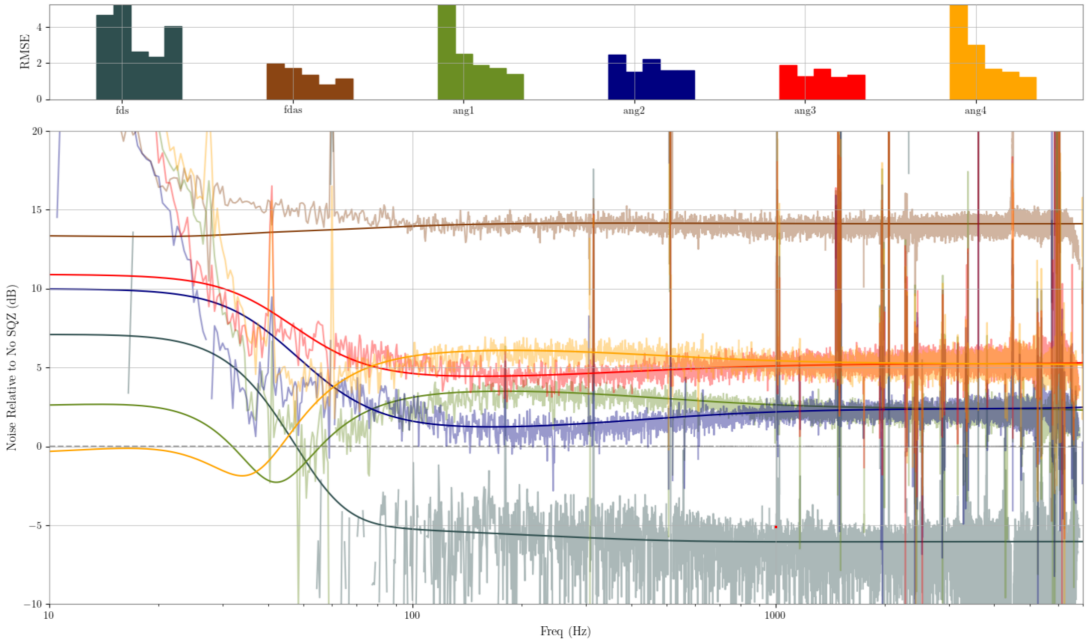

Figure 5: Frequency Dependent fits

value under 2 dB between 40 and 6000 Hz. The frequency dependent data fits nicely between 100 and 1000 Hz with an RMSE under 2 dB. Below 70 Hz, there is significant deviation between the quantum noise models and the DARM spectra. As there was no way to recreate this low frequency behavior using the free parameters, on further investigation, we determined this discrepancy was most likely do to non-stationary low frequency noise which can be seen in DARM spectra during the time of measurement [9]. The complete fitted parame-

ters are listed in Tables 3 and 4. The fits suggest that between the two measurements, there is a drop in the injected squeezing and a change in SEC detuning, as well as the IFO-OMC mode mismatch and mismatch phase. The decrease in injected squeezing matches the overall decrease in mean squeezing between the two dates while the increase in SEC detuning matches changes done the day before the frequency independent measurements were taken [10]. While the change in mode matching is more difficult to pin to a particular source, it could be a result in thermalization changes between the two measurements or small changes in the alignment.

Filter Cavity Detuning	—
Injected SQZ	12.79 dB
Injection Loss	8.4%
SEC Detuning	0.044°
Filter Cavity Mismatch	—
Filter Cavity Mismatch Phase	—
IFO-OMC Mismatch	5.7%
IFO-OMC Mismatch Phase	-18.23°
SQZ-OMC Mismatch	3.63%
SQZ-OMC Mismatch Phase	-65.27°
Arm Power	308 kW
Phase Noise	0.027 rad

Table 3: Frequency independent fitted parameters

Filter Cavity Detuning	-23.8 Hz
Injected SQZ	15.46 dB
Injection Loss	8.4 %
SEC Detuning	-0.31°
Filter Cavity Mismatch	2.4 %
Filter Cavity Mismatch Phase	41.31°
IFO-OMC Mismatch	3.3 %
IFO-OMC Mismatch Phase	-34.84°
SQZ-OMC Mismatch	3.63%
SQZ-OMC Mismatch Phase	-65.27°
Arm Power	308 kW
Phase Noise	0.027 rad

Table 4: Frequency dependent fitted parameters

MCMC Fitting

With an estimation of the squeezing parameters for both data sets, we can conduct a more thorough investigation of the parameter space through Markov Chain Monte Carlo simulations (MCMC). MCMC simulations allow the estimation of high dimensional posterior probability distributions through the use of Markov chains. While there are many flavours of MCMC algorithms, we will use the Emcee sampler which implements an affine-invariant ensemble sampler [11]. This sampler provides broad exploration of the parameter space through the use of multiple walkers which can be run in parallel. As opposed to previous implementations of MCMC fitting on quantum noise modeling, squeezing angle will not be fed as a free parameter. Instead, in each step of the simulation, squeezing angle will be swept and fixed at the angle that minimizes shot noise around 2000 Hz, mimicking the process used in hand-fitting. All other squeezing angles will remain free parameters. Initial prior distributions for most parameters will be set centered around the hand-fitted values for each data set. IFO-OMC, SQZ-OMC, and Filter cavity mismatch phases, however, will be given a larger range in order to explore their degeneracy. As generating GWINC models over a large array of frequencies is a computationally intensive process, we need to re-bin our spectra from linearly spaced frequency bins to logarithmically spaced bins in order to

speed up quantum noise calculations as well as balance the weight of low frequency and high frequency fitting in likelihood calculations. To ensure re-binning doesn't filter out noise, we will implement an algorithm which conserves the total spectral energy within each bin, used in previous MCMC studies [1]. Using this method, the original 8000 linearly spaced bins can be reduced to 200 logarithmically spaced bins, shown in Fig. 6, dramatically speeding up quantum noise calculations. We run MCMC simulations with 300 walkers, each performing 4000 steps to ensure proper convergence. The first 200 steps are discarded to remove influence from initial conditions. Corner plots for frequency independent data are shown in Fig. 7.

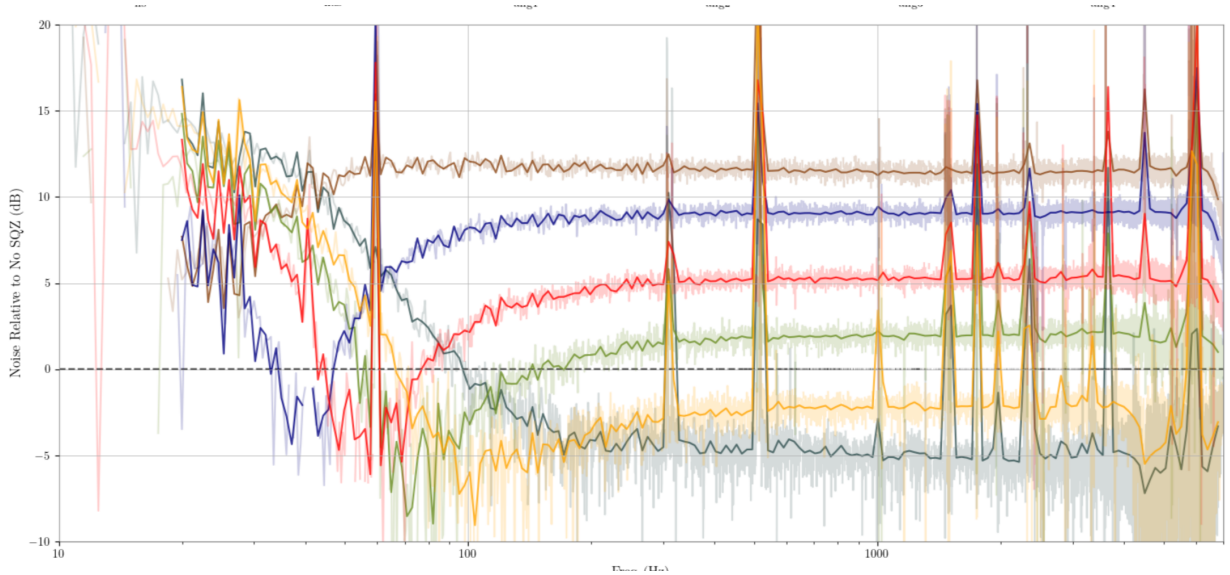

Figure 6: Logarithmically binned DARM overlayed over original linearly binned data

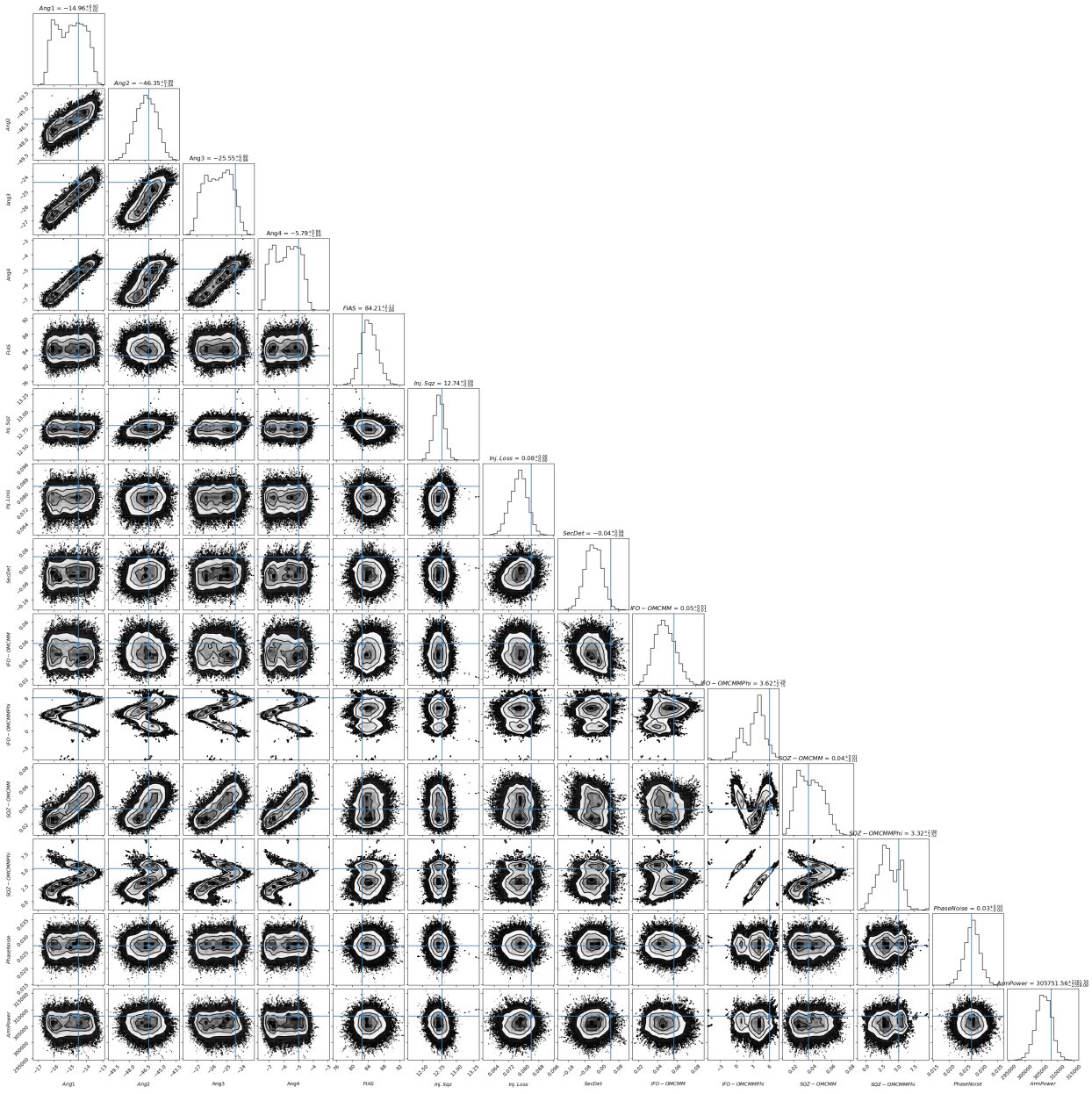

Figure 7: Frequency Independent MCMC results. Handfitted values are marked by the blue lines

We can see that most parameters are well localized by the algorithm. The corner plot highlights how the mode mismatch phases exhibit degeneracy with the squeezing angles, as well as with their respective mode mismatch parameter, seen by the S shaped distributions. We can compare this behavior to the frequency dependent results, shown in Fig. 8.

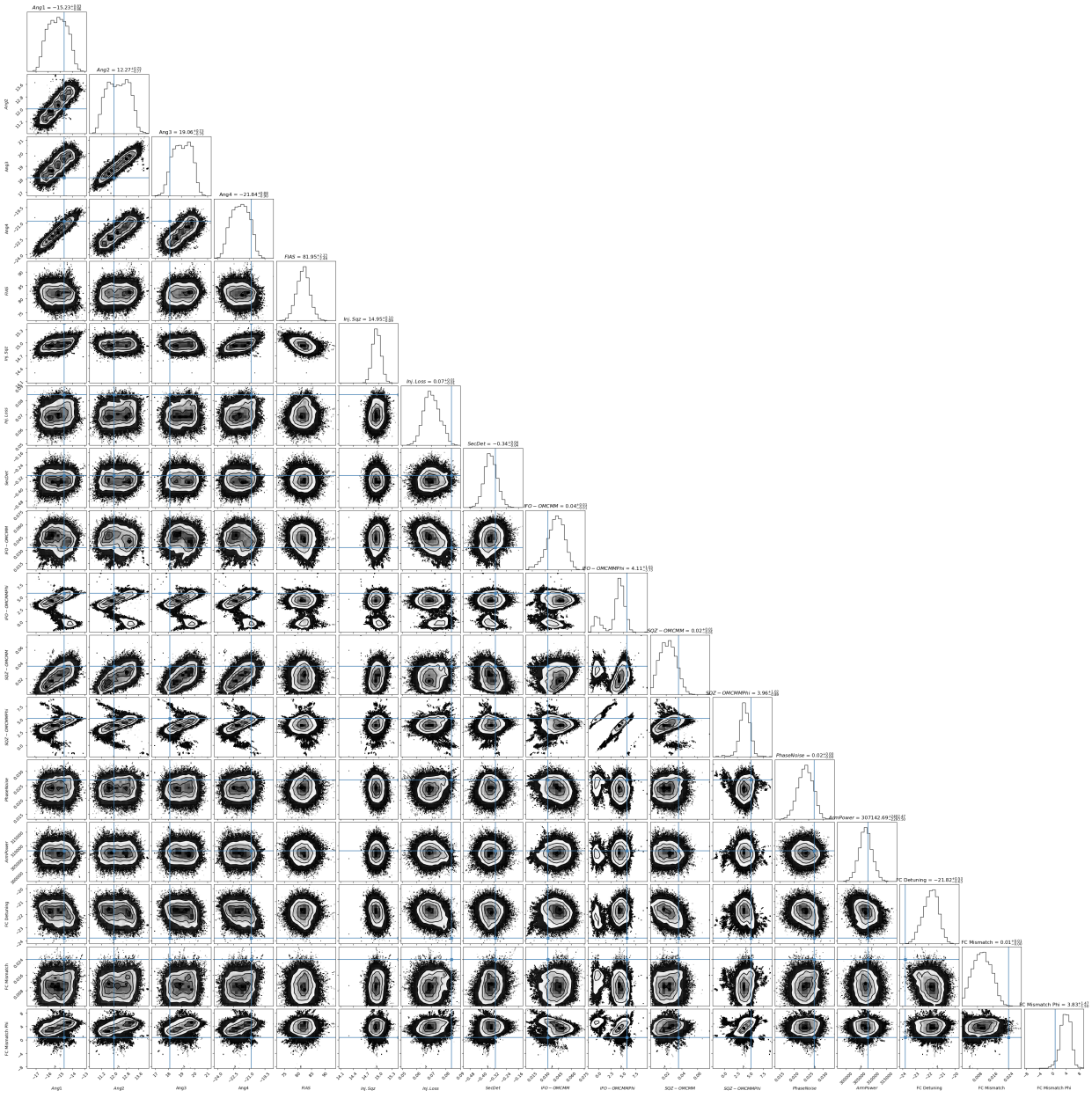

Figure 8: Frequency Dependent MCMC results. Handfitted values are marked by the blue lines

While degeneracy is still present, it seems to be better constrained compared to the frequency independent results, suggesting that the inclusion of the filter cavity parameters may be able to better constrain the mismatch phase parameters. Ultimately, this degeneracy suggests that in order to fully localize the mismatch phase parameters, we need to better localize the squeezing angles. Future work could explore fixing squeezing angle by converting from the measured CLF angle to squeezing angle[12]. Aside from the mismatch phase parameters, all other parameters are nicely localized and fall within the ranges predicted by the hand-fitted models. The frequency independent and dependent MCMC parameters results are listed in Tables 5 and 6 alongside the hand-fitted estimates.

Parameter	Hand-Fitted	MCMC
Injected Squeezing	15.46 dB	$14.95^{+.010}_{-.09}$ dB
Injection Loss	8.4%	7^{+1}_{-1}%
SEC Detuning	−0.31 deg	$-0.34^{+0.04}_{-0.04}$ deg
IFO - OMC MM	3.3%	4^{+1}_{-1}%
IFO - OMC MM Phase	5.68 rad	$4.11^{+1.01}_{-3.73}$ rad
SQZ - OMC MM	3.6%	2^{+1}_{-1}%
SQZ - OMC MM Phase	5.14 rad	$3.96^{+1.02}_{-0.89}$ rad
Phase Noise	27 mrad	20 mrad
Arm Power	308 kW	$307^{+2.4}_{-2.3}$ kW
FC Detuning	−23.8 Hz	$-21.82^{+0.53}_{-0.63}$ Hz
FC MM	2.4 %	1^{+1}_{-0}%
FC MM Phase	0.720 rad	$3.83^{+1.47}_{-1.50}$ rad

Table 5: Frequency dependent squeezing fitted parameters versus MCMC results.

Parameter	Hand-Fitted	MCMC
Injected Squeezing	12.79 dB	$12.74^{+.08}_{-.08}$ dB
Injection Loss	8.4%	8%
SEC Detuning	0.044 deg	$-0.04^{+0.04}_{-0.04}$ deg
IFO - OMC MM	5.7%	5^{+1}_{-1}%
IFO - OMC MM Phase	5.97 rad	$3.62^{+1.29}_{-2.75}$ rad
SQZ - OMC MM	3.6%	4^{+1}_{-1}%
SQZ - OMC MM Phase	5.14 rad	$3.32^{+2.08}_{-1.52}$ rad
Phase Noise	27 mrad	30 mrad
Arm Power	308 kW	$306^{+2.3}_{-2.4}$ kW

Table 6: Frequency Independent squeezing fitted parameters versus MCMC results

Part Two: Finesse Modeling

In the quest for ever higher squeezing levels at LIGO detectors, one source of loss, mode mismatch, fundamentally limits the injection efficiency of the quantum squeezing system. While in practice, mode mismatch between the squeezer and the interferometer is a notoriously complex source of loss, fundamentally, it is the result of spatial mismatch between squeezed vacuum and the fundamental modes of the interferometer and output mode cleaner (OMC), ultimately degrading the amount of squeezed vacuum injected [13]. The total frequency dependent mode mismatch loss can be broken down into the complex mode mismatch between the squeezer and the filter cavity, squeezer and interferometer, and between the squeezer and the output mode cleaner. Currently, mode mismatch to the filter cavity is minimized through adjustments to the ZM2 PSAM, while mode matching to the interferometer is controlled through the ZM4 and ZM5 PSAMS which guide the squeezed beam from the vacuum optical parametric oscillator injection platform (VIP) and into the output Faraday isolator. Scanning the radius of curvature of both mirrors can optimize the beam parameter exiting the squeezer for better mode matching to the interferometer, yet this process can be time consuming [14, 15, 16]. Since mode matching is highly sensitive to the thermalization of the interferometer, changes in CO2 alignment can often necessitate a re-scan of the ZM4 and ZM5 PSAMS, costing precious observing time [15]. Hence, there is a need for a model of the squeezing output and filter cavity path in order to predict mode mismatch and better inform PSAM settings.

Modeling the Squeezing Output Path

The Finesse simulation will be informed from a set of beam scans taken during the A+ detector upgrade [17]. These scans give measurements of the beam radius in both the horizontal and vertical direction before the ZM2, ZM4, and ZM5 PSAMS, allowing for the calculation of the beam parameter to the filter cavity and exiting the squeezer by fitting the measurements to a Gaussian beam profile. The radius of a Gaussian beam as a function of distance from the beam waist position, z_0, is given by the equation:

$$w(z) = w_0\sqrt{1 + \left(\frac{(z - z_0)}{z_r}\right)^2} \tag{1}$$

where z_r is the Rayleigh range, defined as:

$$z_r = \frac{\pi\omega_0^2}{\lambda} \tag{2}$$

This defines a complex q-parameter which determines the beam propagation.

$$q(z) = (z - z_0) + z_r i \tag{3}$$

The beam scans determine the beam parameter incident on ZM4 through measurements of the horizontal and vertical beam radius at three points before the ZM4 mirror (See appendix B). A flat diverting mirror is then placed in-front of ZM4 and three additional measurements are taken at distances beyond ZM4. The points are fitted to equation (1) to determine the beam waist radius and distance from ZM4.

	Horizontal	Vertical
Beam Waist Radius (μm)	630.544	674.651
Waist Position (m)	-1.615	-1.334

While this beam parameter will serve as the starting point for our Finesse simulation, in order to accurately simulate the beam's response to the ZM4 and ZM5 variable radii of curvature, a mapping of applied voltage to radius of curvature for both the ZM4 and ZM5 mirrors is necessary. This was calculated from beam scan measurements after ZM4 with the beam profiler 400mm away from ZM5. The PZT voltage applied on ZM4 was then increased from 0V to 200V and the beam size at each voltage was recorded. Since there is known hysteresis with the PSAMS response to PZT voltage, the beam profile was also recorded during a sweep from 200V down to 0V [18]. It is more informative to look at the strain gauge voltage, which is a more constant indicator of the radius of curvature [19]. Using the beam profile, the radius of curvature of ZM4 in both the horizontal and vertical planes can be calculated. Due to a discrepancy between the designed and implemented distance between ZM4 and ZM5, the PSAM calculation was redone. The original calculation was done with the distance between ZM4 and ZM5 as 1681 mm, while new corrections measure the distance as 1691 mm [20]. This places the beam profiler 1cm closer to ZM5 during the PSAM scan. Recalculating the beam scans gives us a linear conversion between the strain gauge voltage and the ZM4 defocus in both the horizontal and vertical direction, seen in Fig. 9.

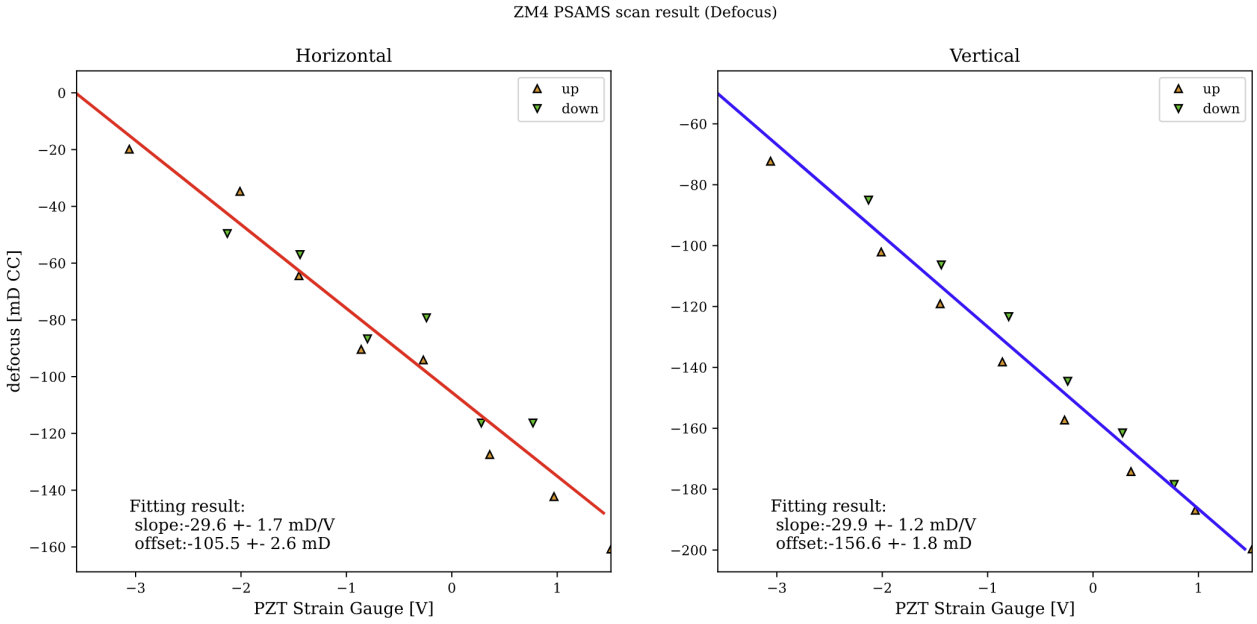

Figure 9: ZM4 Defocus as a function of ZM4 strain voltage. Due to hysteresis, measurements are taken with both an increasing and decreasing PZT voltage, represented by the up and down arrows. Uncertainties are calculated using the covariance matrix of the linear fit.

Converting from defocus to radius of curvature and propagating the uncertainty in the fits give us expressions for the radii of curvature of ZM4 as a function of strain gauge voltage.

$$RoC(v_s) = \left(\frac{2}{mv_s + b} \pm 2 \cdot \frac{\sqrt{\Delta b^2 + \Delta m^2 v_s^2}}{(mv_s + b)^2} \right) \cdot 10^3 \tag{4}$$

Here b is the fit offset in mD and m is the fit slope in mD/V. This equation can be tested against the PSAM scan data by comparing the calculated radius of curvature at each strain gauge voltage to the radius of curvature inferred from the data.

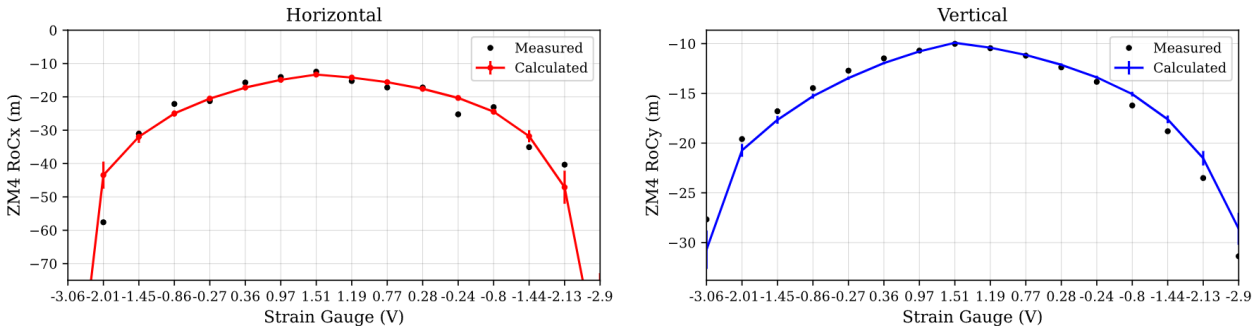

Figure 10: Zm4 RoCx and RoCy as a function of strain gauge voltage. It is evident from the asymmetry between the increasing and decreasing strain voltage that some hysteresis is still present.

While there is significant deviation towards lower values of strain gauge voltage, around the optimal operating point (0-1.5V), the fit is fairly consistent. We can now begin to build a Finesse model based on these measurements.

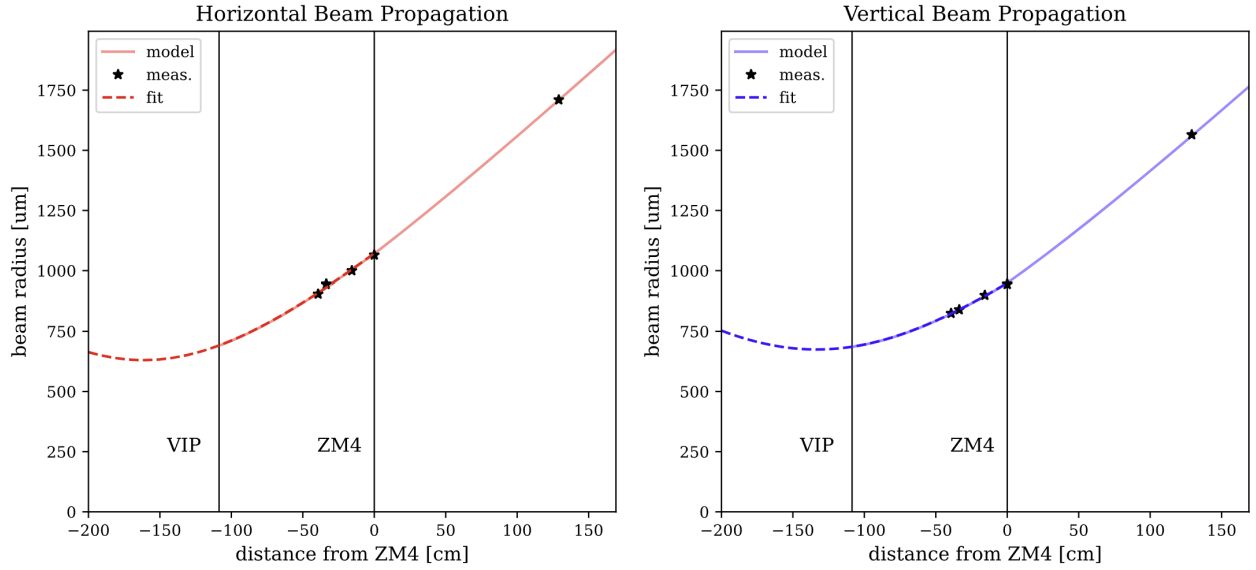

Figure 11: Vertical and horizontal beam propagation around ZM4. The dotted line represents the fitted beam profile while the solid line represents the finesse simulation results.

Figure 11 shows the Finesse beam propagation with the PSAM set to 0V (-3.06 V Strain gauge). Since our estimate for the ZM4 radius of curvature will be very inaccurate for such a low strain voltage, we instead use the horizontal radius of curvature of -100.76 m and vertical

radius of curvature of -27.67 m which were calculated from the measurements.

We now move forward and model the beam around ZM5. The same procedure of using a diverting mirror to measure the beam size before and after ZM5 is used to get the beam parameter incident on ZM5. Based on the measurement logs, the ZM4 PSAM was set with a strain voltage of -0.79 V [21]. Calculating the radius of curvature using equation 4 gives us:

$$RoC_x = -24.36 \pm 0.67m \qquad RoC_y = -15.04 \pm 0.23m$$

Another PSAM scan was done, now with the beam profiler placed 260mm from the edge of the HAM7 table. The discrepancy in the ZM4 to ZM5 distance again needs to be taken into account as the distance from the profiler to ZM5 was calculated using the design distance between ZM4 and ZM5 (1681mm) and estimates from the HAM7 optical layout document [22]. Recalculating the PSAM scan gives us a relationship between strain gauge voltage and ZM5 defocus.

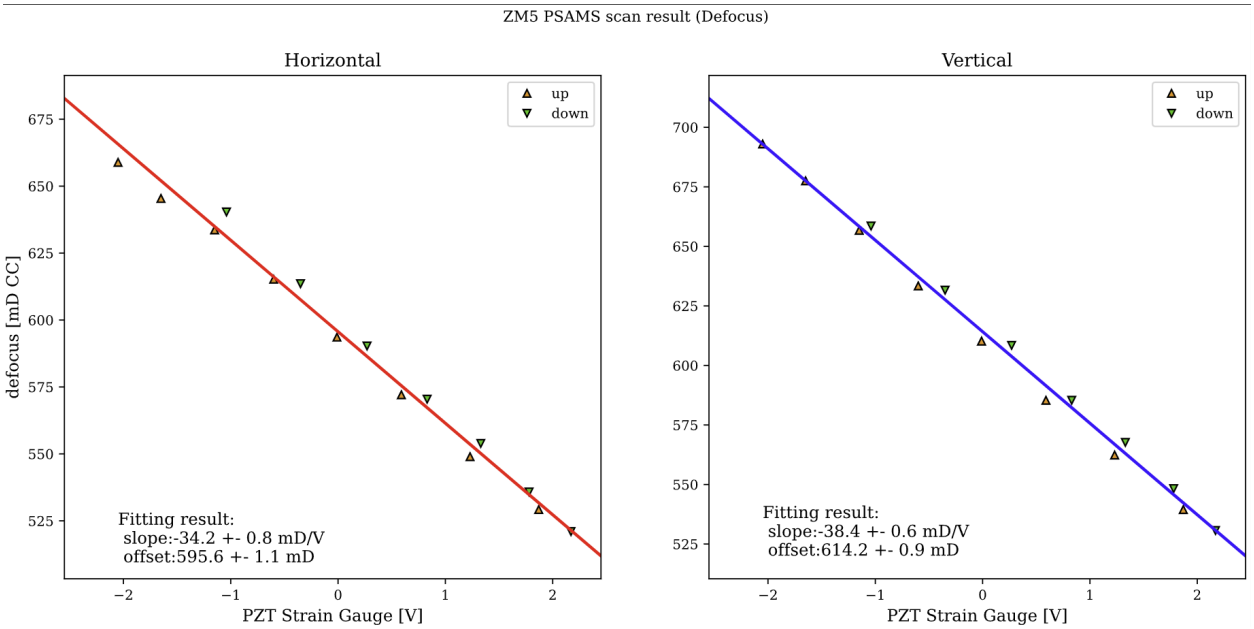

Figure 12: ZM5 Defocus as a function of strain gauge voltage

We can now connect ZM4 and ZM5 and test the Finesse beam propagation, shown in Fig. 13. While the model is relatively consistent, there is notable deviation in the horizontal beam size incident on ZM5 and the vertical beam waist location. This is most likely due to inaccuracies in the ZM4 radii of curvature. This can be checked by calculating the ZM4 horizontal radius of curvature using the individual beam measurements before ZM5, shown in Table 7. Excluding the outlier point at z = -137mm, we get an average horizontal radius of curvature of -33.90 m and average vertical radius of curvature of -15.94. The calculated horizontal radius of curvature is much larger than the horizontal radius of curvature of -24.36m predicted from the PSAM scan, suggesting some error. Since this error is only evident in the horizontal radius of curvature, it is hard to pin this to a discrepancy in either

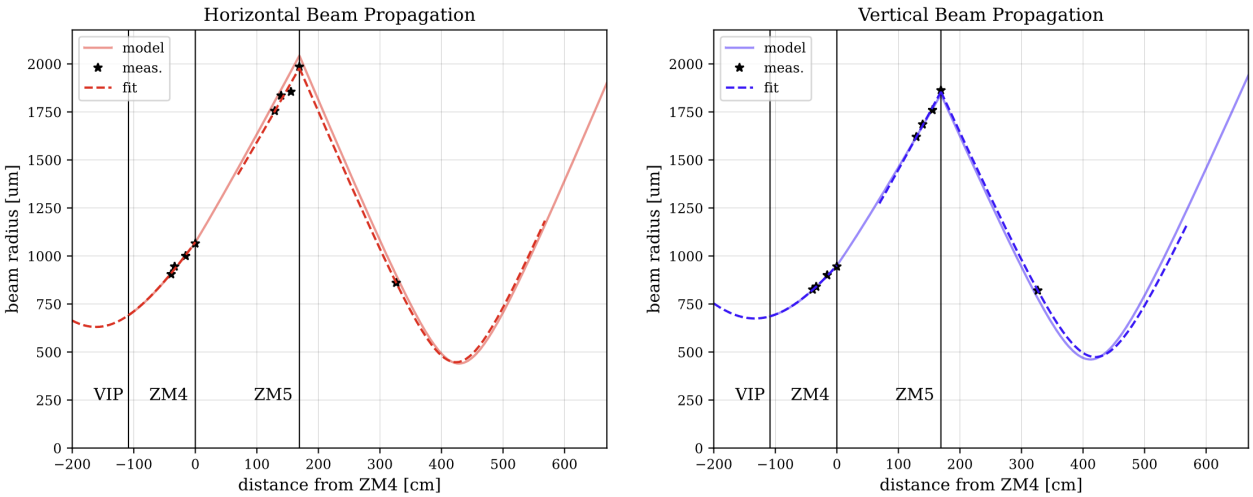

Figure 13: Vertical and horizontal beam propagation through ZM4 and ZM5. ZM4 RoC is set assuming a strain voltage of -0.79 V while ZM5 RoC is set assuming 0V PZT (-2.05 V strain).

Z [mm]	$w_x[\mu m]$	$w_y[\mu m]$	$RoC_x[m]$	$RoC_y[m]$
-400	174	162	-37.53	-16.79
-297	183	168	-28.90	-15.91
-137	185	176	-80.44	-17.33
0.0	198	186	-34.60	-15.04
80.0	204	191	-30.32	-15.27
160.0	206	195	-38.16	-15.31

Table 7: Beam measurements after ZM4 and the calculated ZM4 radii of curvature. Measurement distance is relative to the ZM5 position

the measured distances, or distances used in the model. It is possible that the beam profiler was slightly misaligned, causing the six horizontal beam measurements before ZM5 to be inaccurate.

Tracking errors

While these models are fairly accurate, small deviations could originate from inaccuracies in the distances used. We will focus on three distances that could have introduced error:

- Error in the distance between ZM4 and ZM5
- Error in the location of the ZM4 PSAM measurement location
- Error in the location of the ZM5 PSAM measurement location

We will start by sweeping the distance between ZM4 and ZM5. Since both PSAM scan measurement positions are derived from this distance, they will need to be recalculated at

each tested distance. For each distance, we can run the Finesse model at each of the ZM4 and ZM5 radii of curvature tested by the PSAM scan and calculate the percentage error between the beam waist size and location after ZM5. Due to the unknown radius of curvature of ZM4 during the ZM5 PSAM scan, we will recompute it for each distance by again averaging over the calculated curvature based on the five measurements before ZM5. Figure 14 shows the result of plotting the average percentage error versus distance from ZM4 to ZM5.

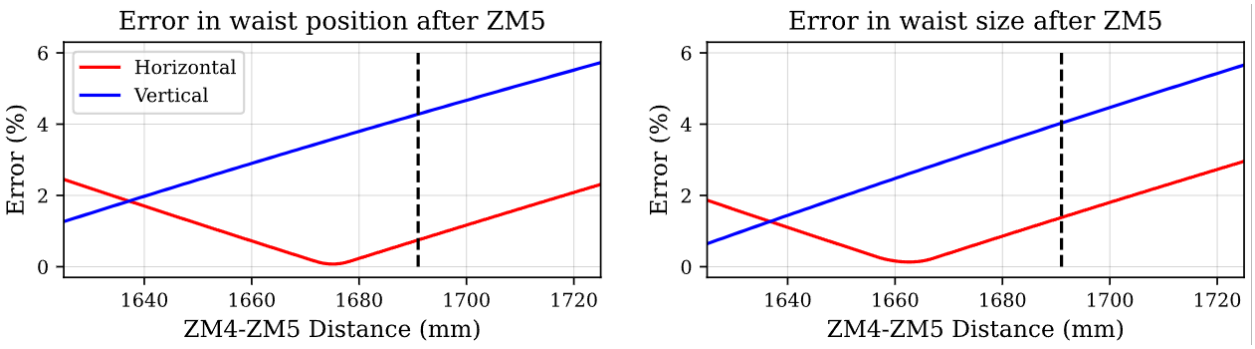

Figure 14: Percentage error in the beam waist position and size after ZM5 as a function of the distance between ZM4 and ZM5. The recorded distance is marked by the black dotted line.

The plot shows that the model prefers a smaller distance between ZM4 and ZM5 with the error in the horizontal waist position reaching a minimum error of 0.007% at a distance of 1675mm. While it is not unreasonable for there to be a 16 mm error in the ZM4 to ZM5 distance, especially given the original design distance of 1681 mm, it does not completely fix the issue as the vertical waist size and position do not reach below 2% error until beyond 1640mm, which would be an unreasonable error in position. We can similarly sweep the

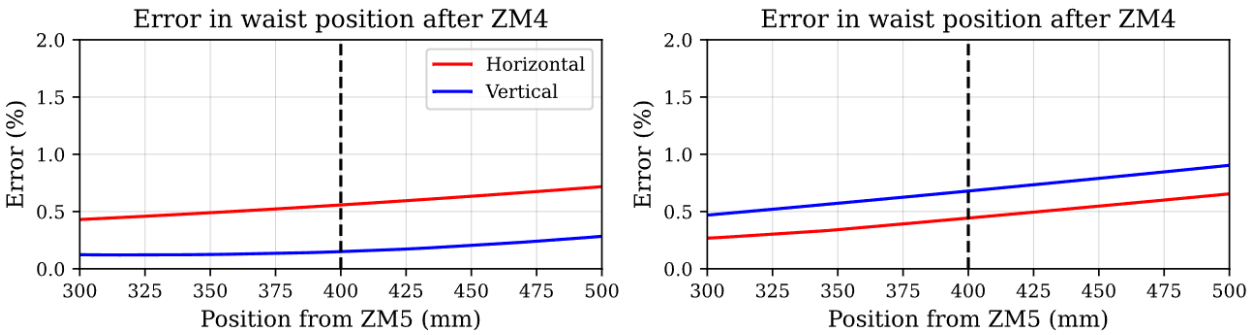

Figure 15: Error in beam waist and location as a function of distance between beam profiler location during ZM4 PSAM scan, measured from ZM5. The recorded distance is marked by the dotted line.

ZM4 PSAM and ZM5 PSAM measurement locations to generate similar error plots, seen in Fig. 15 and 16. There does not seem to be enough of a significant trend in the error of these two measurement locations to explain any discrepancies. Ultimately, these results suggest that there could be a small discrepancy in the distance between ZM4 and ZM5, but is not enough to completely explain the error. For now, we will stick with a distance of 1691 mm between ZM4 and ZM5 and continue the beam propagation.

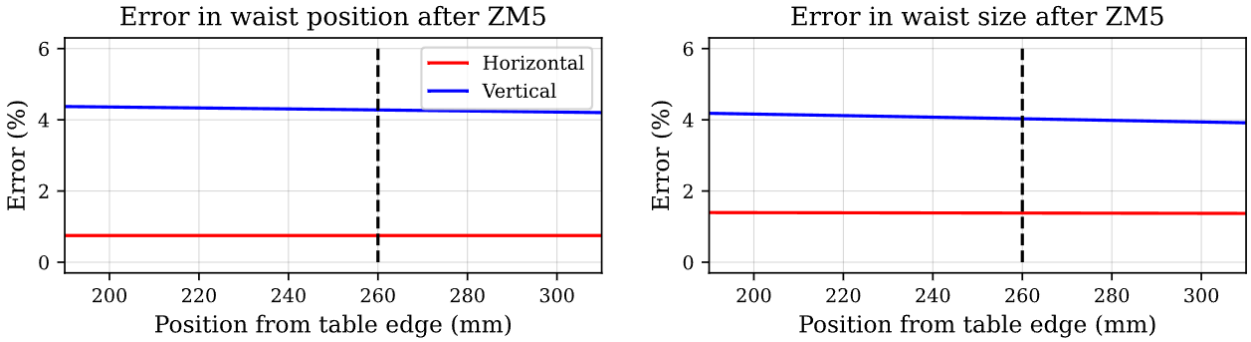

Figure 16: Error in beam waist and location as a function of distance from from beam profiler to HAM7 edge during ZM5 psam measurements.

Mode Matching to the OMC

Using the output of our ZM4 and ZM5 model, we can propagate our beam into HAM6 and to the output mode cleaner (OMC) and calculate the mode mismatch. We will reflect the beam off the signal recycling mirror inner surface, bypassing the interferometer. The beam propagation can be seen in Fig. 17.

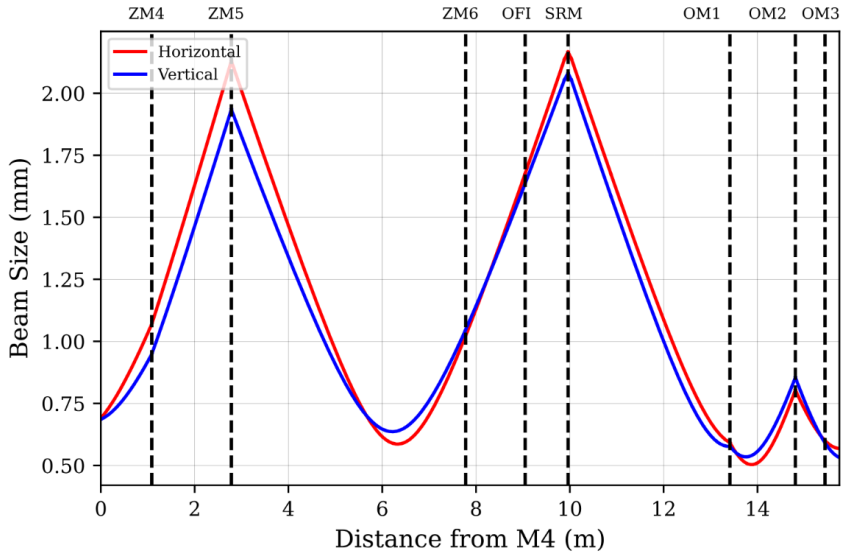

Figure 17: Beam propagation from before ZM4 to OMC. The beam is reflected off the inner surface of the SRM mirror. ZM4 and ZM5 PSAMS are both set to 1V on strain gauge.

Taking the beam parameter at the entrance to the OMC, we can calculate the overlap integral with the OMC eigenmode, calculated by finesse to be,

$$q_x = -0.1407 + 0.7075i \quad \text{and} \quad q_y = -0.1407 + 0.7101i$$

The electric field overlap integral for two Gaussian beams with beam parameters q_{1x}, q_{1y} and q_{2x}, q_{2y} can be analytically solved (see appendix A) as:

$$O = \sqrt{\frac{(q_{1x} - q_{1x}^*)(q_{1y} - q_{1y}^*)(q_{2x} - q_{2x}^*)(q_{2y} - q_{2y}^*)}{(q_{1x} - q_{2x}^*)(q_{1y} - q_{2y}^*)(q_{1x}^* - q_{2x})(q_{1y}^* - q_{2y})}} \tag{5}$$

The mode mismatch will then be one minus the electric field overlap. Assuming a ZM4 and ZM5 strain of 1V, the mode mismatch calculated at the output of the OMC IC mirror is 1.66%. A OMC mode scan taken shortly after the beam profiling estimates mode matching to be 98% (2% mismatch) [23], agreeing with our model. We can now scan ZM4 and ZM5 strain gauge to get a mapping of the mode mismatch seen in Fig. 18 It is important to

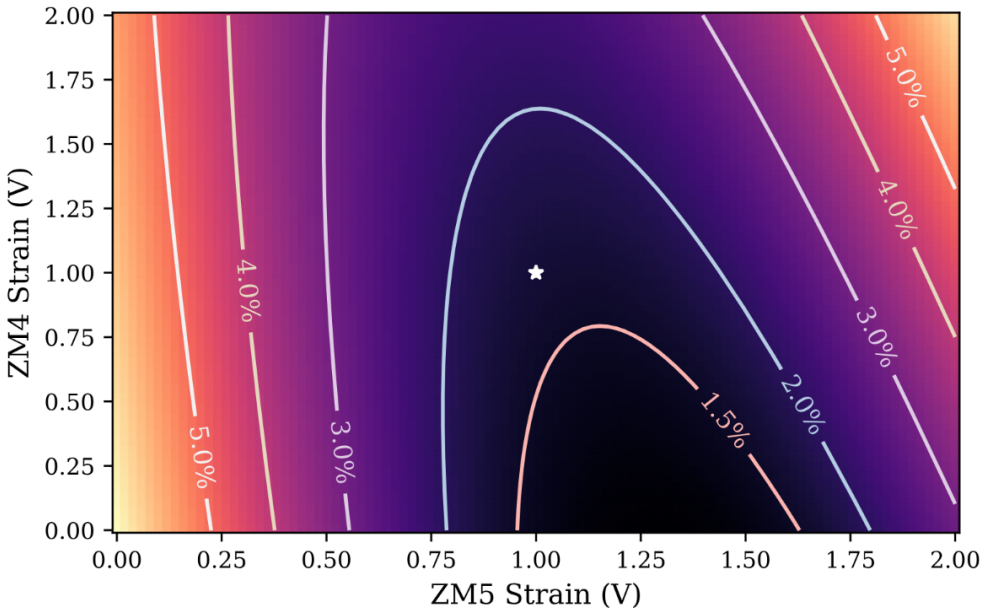

Figure 18: Mode mismatch between the squeezer and the OMC as a function of ZM4 and ZM5 strain voltage. The white star marks our current operating region of around 1V on both ZM4 and ZM5, resulting in a predicted mode mismatch of 1.66%.

note that this model assumes that the squeezed beam is perfectly aligned with the OMC. In reality, the mismatch also depends on the beam alignment which is not included in the model. This could be the reason for the mismatch being lower than the 3-4% mismatch predicted from quantum noise modeling. This difference could also be due to a change in ZM2 strain voltage from -2.7V to -2.3V between now and the time of beam profiling, resulting in the beam exiting the VIP to change. Incorporating this into our Finesse model necessitates a full model of the filter cavity path as well as the VIP.

Modeling the Filter Cavity Path

Beam scans were also taken around the ZM2 PSAM which is used for optimizing mode matching to the filter cavity. The beam parameter exiting the VIP, incident on ZM2, was calculated using nine beam measurements before ZM2.

	Horizontal	Vertical
Beam Waist Radius (μm)	211.507	212.818
Waist Position (m)	-1.509	-1.513

PSAM beam measurements were taken with the beam profiler 830mm away from ZM2 giving us a conversion from strain gauge to radius of curvature, shown in Fig. 19.

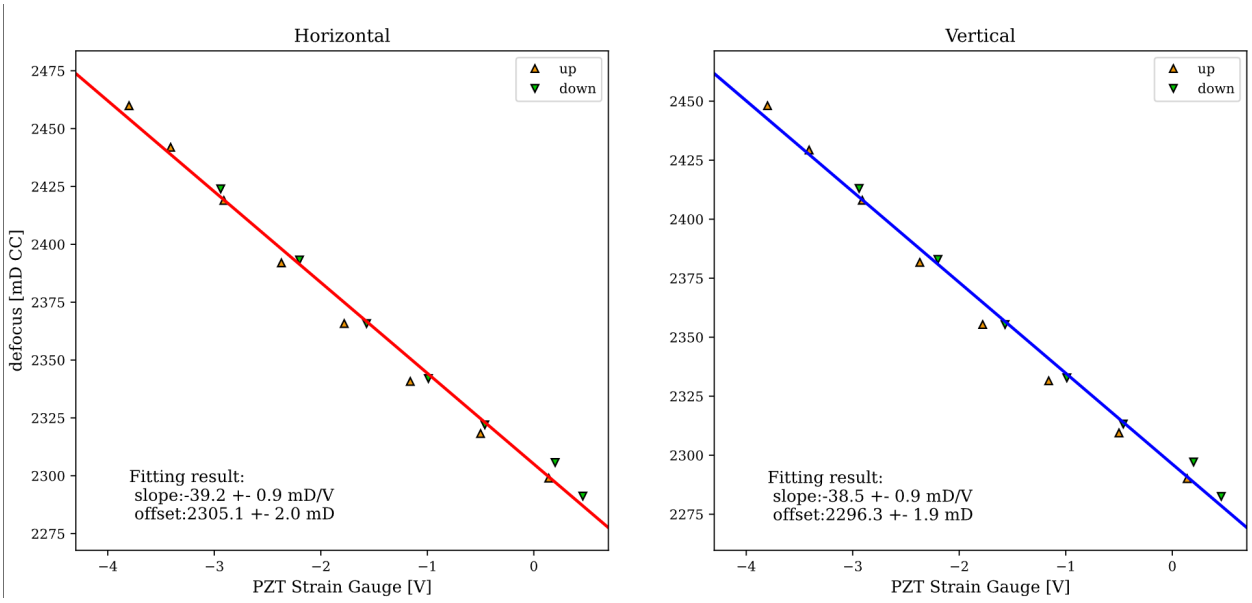

Figure 19: ZM2 Defocus as a function of strain gauge voltage.

We can now compare our model to measurements taken with the ZM2 PSAM set at -3.80V strain gauge voltage. Using Eqn. (4), this gives us:

$$RoC_x = 0.815 \pm 0.001m \quad RoC_y = 0.819 \pm 0.002m$$

The Finesse model result is shown in Fig. 20.

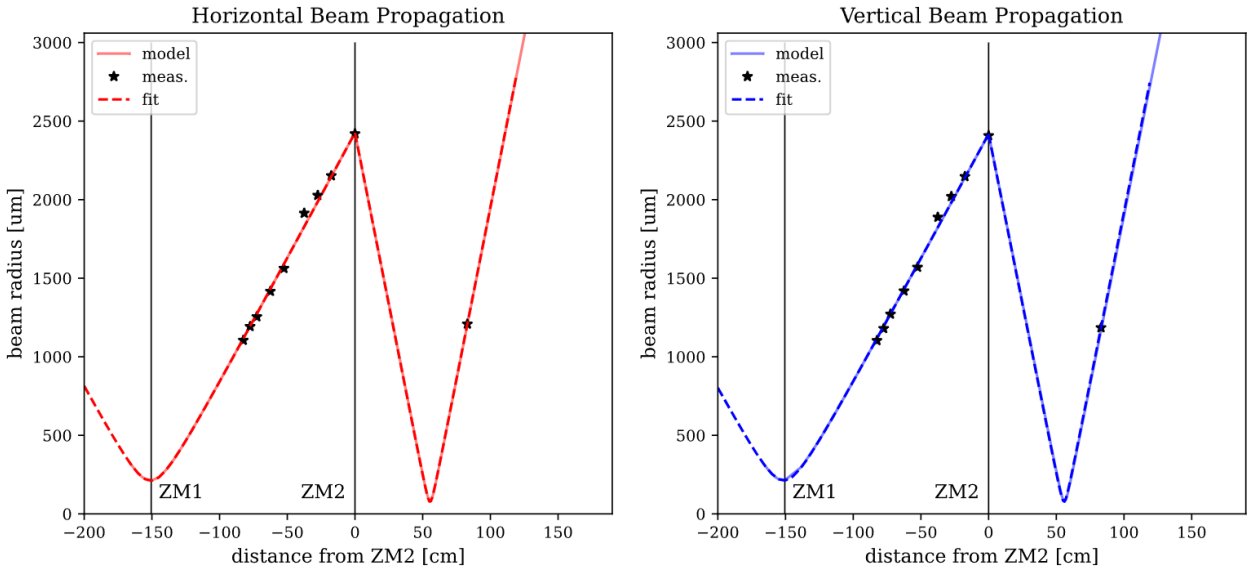

Figure 20: Beam propagation from the VIP through ZM2 towards the filter cavity

The accuracy can be assessed by comparing the predicted beam waist size and position after ZM2 with the measurement fits, given in in table 8.

	Model	Measurement
Horizontal Beam Waist Radius (μm)	77.52	77.43
Horizontal Waist Position (m)	0.55	0.55
Vertical Beam Waist Radius (μm)	78.54	78.11
Vertical Waist Position (m)	0.56	0.56

Table 8: Modeled beam waist size and position compared to beam waist size and position calculated from beam scans.

Filter Cavity Mode Matching

With an accurate model of the beam around ZM2, we can propagate it towards the filter cavity and calculate the mode mismatch. The complex beam parameter of the filter cavity fundamental mode at the filter cavity input mirror AR surface can be determined from the propagation of the filter cavity fundamental mode to be $q_{fc} = 2.222 + 0.0186i$. Using Finesse, we can calculate the q-parameter of the squeezed beam on the FC1 mirror. The mode mismatch can then be plotted as a function of ZM2 strain gauge voltage, seen in Fig. 21. The result suggest an optimum ZM2 strain gauge of -0.29 V which gives a minimum

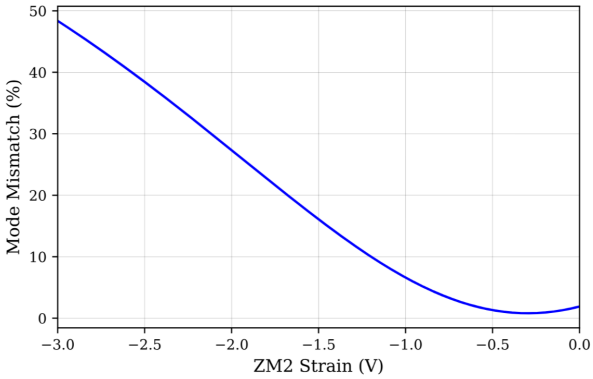

Figure 21: Filter cavity mismatch as a function of ZM2 Strain Gauge. The ZM2-ZM3 distance used is 1.835m.

mode mismatch of 0.81 %. This result is not consistent with the current operating strain gauge voltage of around -2.3V [24, 25], suggesting an error somewhere in the Finesse model. Since our output beam from ZM2 is consistent with the beam scan measurements, there is most likely an error in the distance between ZM2 and ZM3, or between ZM3 and the filter cavity. We can test various values for the distance between ZM2 and ZM3 and plot each mode mismatch curve, seen in Fig. 22. With a current ZM2 strain value of -2.3 V [24], this result suggests that the total distance between ZM2 and the filter cavity is shorter by around 2 cm. This could be due to a combination of error in both the ZM2 to ZM3 distance, and in the ZM3 to FC1 distance. The PSAM scans around ZM2 estimate the distance between ZM2 and the Filter cavity as 2.795 m using the beam-size of the back reflected from the filter cavity [17]. Our current model assumes a total distance of 2.8264 m between ZM2 and FC1 (1.8349m from ZM2 to ZM3 and 0.9905m from ZM3 to FC1), resulting in a 3.1cm error. We will assume this discrepancy is between ZM2 and ZM3 and rerun our model using a decreased distance of 1.805m. Using this distance and a strain gauge voltage of -2.3V,

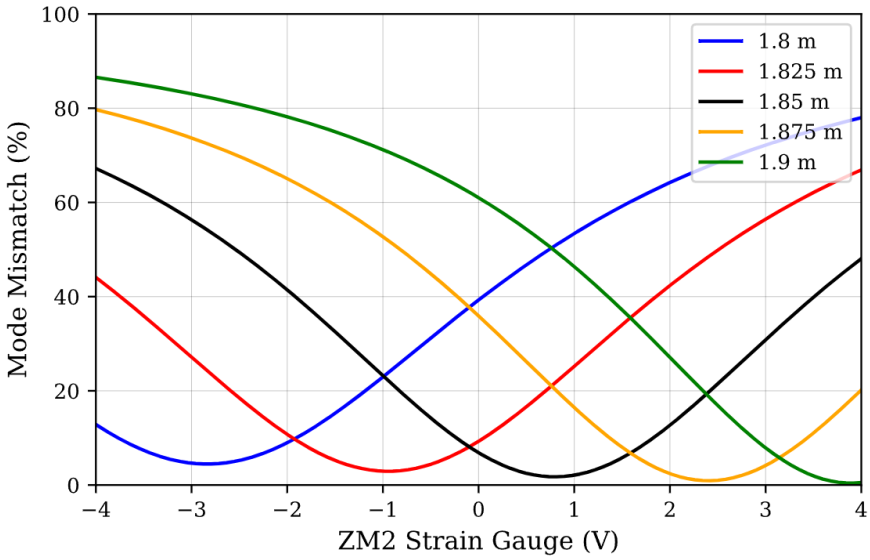

Figure 22: Mode mismatch as a function of ZM2 strain gauge voltage for 5 different ZM2-ZM3 distances. Decreasing the ZM2-ZM3 distance moves the minimum mode mismatch towards the used ZM2 operating voltage of around -2.3V.

we get a mode mismatch of 1.05%. Note however that following these measurements, the ZM2 PSAM was set at -2.7V strain and not decreased down to around -2.1 V until January of 2023 [26]. Using -2.7V strain gauge voltage, the mode mismatch to the filter cavity is 0.88%. It is not clear why the PSAM was decreased from -2.7V, but it may suggest that this distance estimation may not be entirely accurate, assuming that -2.3V is optimum for mode matching to the filter cavity.

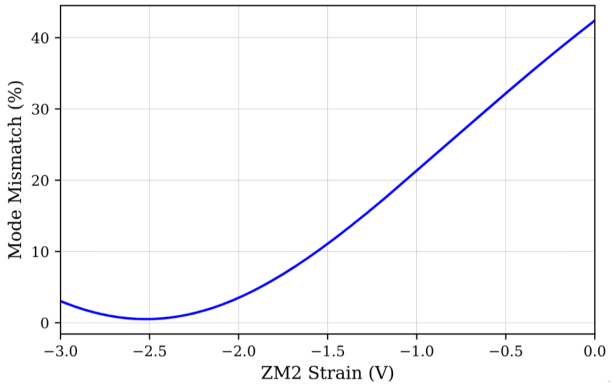

Figure 23: Filter cavity mismatch as a function of ZM2 Strain Gauge with a ZM2 to ZM3 distance of 1.805 m.

Modeling the VIP

Ideally, by modeling the path from the filter cavity to ZM4, we should be able to predict how the change in ZM2 strain affected the beam parameter exiting the VIP, and the resulting change in mode mismatch. This requires modeling both the VIP A and B path. Using

the model of the OPO [27] by Aaron Jones, we can also propagate the OPO fundamental mode to help asses the model's fit to measurements. The designed path length distances, lens focal lengths, and target beam parameters of the VIP squeezed path are documented in the initial frequency dependent design document [22]. However, during installation many of these parameters were adjusted in response to realistic conditions. Alogs from the installment document many of the changes and updated path lengths [28, 29]. One undocumented change is the removal of the L3 lens which was replaced with a 222mm focal length lens [30]. The design and installation parameters are listed in Table 9.

Name	Designed	Implemented
OPOM1 - A:L1	0.224 m	0.235 m
A:L1-AFI1	0.0675 m	0.074m
AFI1-L2	0.389 m	0.467 m
L2-L3	0.0312 m	0 (L3 removed)
L3 / L2 - A:M3	0.0968 m	0.092m - 0.127m
A:M3 - ZM1	0.158 m	0.0158m
ZM1 - ZM2	1.422 m	1.5052m
A:L1 focus	222 mm	222 mm
A:L2 focus	334 mm	222 mm
A:L3 focus	778mm	—

Table 9: VIP A path design distances and measured distances

The exact position of L2 is unknown as it was placed on a translation stage with a range of 35mm. Figure 24 shows the propagation of both the OPO fundamental mode and the

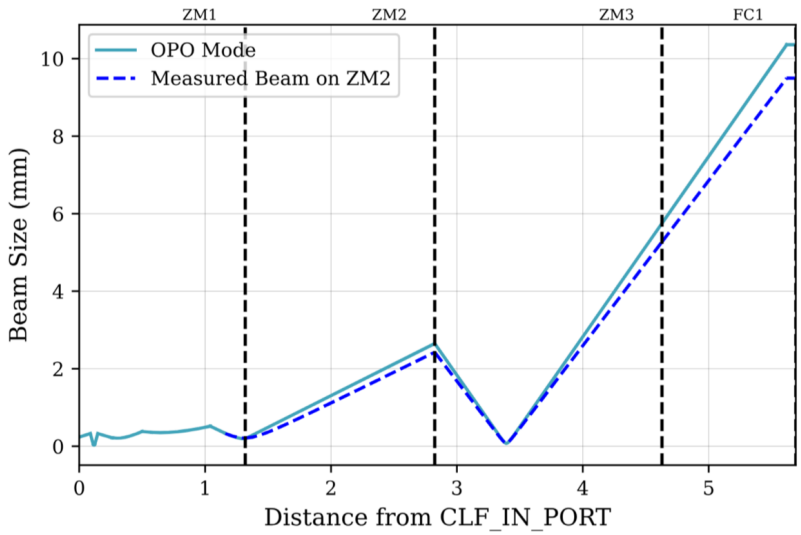

Figure 24: Beam propagation of the OPO mode and ZM2 measurement to the filter cavity with an L2-A:M3 distance of 120mm.

measured beam before ZM2 propagated to the filter cavity. Sweeping the distance between L2 and AM3 and evaluating the mode mismatch between the OPO mode and the ZM2

Name	Designed	Implemented
AFI1-BL1	0.225 m	0.230 m
B:L1-B:L2	0.6625 m	0.733m
B:L2-B:M4	0.1312 m	0.165m
B:L1 focus	778 mm	556 mm
B:L2 focus	1112 mm	1112 mm

Table 10: VIP B path design distances and measured distances

measurement, we find that the minimum mode mismatch is 0.79% with a distance of 120mm between L2 and A:M3.

After reflecting from the filter cavity, the beam is passed back through L2 and into the first Faraday isolator and diverted onto the B path. After passing through lenses B:L1 and B:L2, the beam exits towards ZM4. We can model this path using updated path lengths and lens changes, shown in table 10. Again, sweeping the distance between L2 and A:M3, the minimum mismatch between the ZM2 measurement and the ZM4 measurement is 4.2% with a the L2 translation stage fully forward (91mm between L2 and A:M3). The complete beam propagation is shown in Fig. 25.

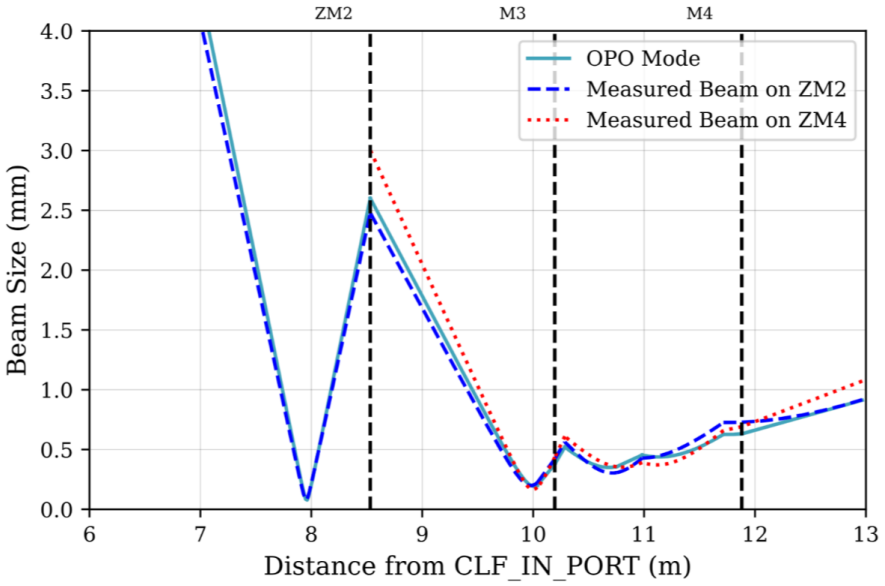

Figure 25: Beam propagation from before ZM2 to ZM4. The back propagated ZM4 measurement is shown by the red dotted trace.

Given the complexity of the path and the many uncertainties in distances, a 4.2 % mismatch is surprisingly good. However, given the distance between ZM4 and the OMC, it is unfortunately not accurate enough to provide an estimation of the current mode matching. We will see if it is possible to fit the two beam parameters together by randomly perturbing the distances between optics and recalculating the mismatch. Figure 26 shows the distribution of observations with under 2% mismatch between ZM2 and ZM4 beams. By perturbing each distance within a 4cm range, the minimum achievable mismatch is 0.08% with the distances shown in table 11. Unfortunately, this requires moving multiple optics by 3 to 4 cm. Since

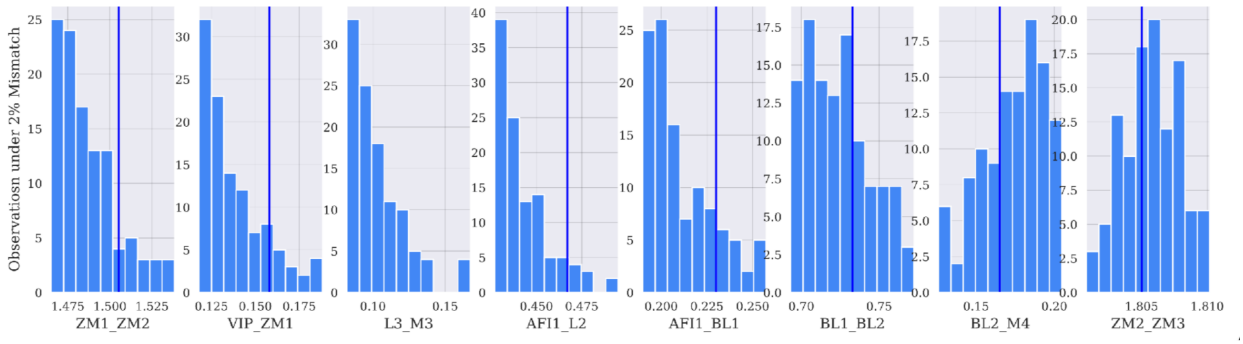

Figure 26: Distribution of optic distances with under 2% mismatch between ZM2 and ZM4 measurements. The measured distance is marked by the blue line.

	Measured	Optimum
ZM2 to ZM3	1.805 m	1.810 m
ZM1 to ZM2	1.5052 m	1.476 m
VIP to ZM1	0.158 m	0.122 m
L3 to M3	0.092 m	0.082 m
AFI1 to BL1	0.230 m	0.202 m
BL1 to BL2	0.733 m	0.705 m
BL2 to M4	0.165 m	0.2040 m

Table 11: Path length distances with minimum mode mismatch to beam parameter before ZM4.

there is no evidence of the VIP path being altered after the path lengths were measured by such a large amount, it is unreasonable to assume a 4cm error in the measured distances. Most likely, this error is due to a combination of uncertainty in distances and uncertainty in ZM2 radius of curvature. Since the beam passes through ZM2 twice, once on the way to the filter cavity and once upon reflection from the filter cavity, our model is especially sensitive to any inaccuracies in the ZM2 strain to RoC conversion and the path length between ZM2 and FC1. Small inaccuracies in the strain conversion as well as inaccuracies in the estimated ZM2 to FC1 length combined with discrepancies in the VIP length could all contribute to the 4.3% mismatch between measurements. To establish confidence in the propagation model, more data is needed to better constrain distances and isolate error.

Conclusion

Two quantum noise modeling tools, interactive fitting and MCMC simulations, were improved and applied on Livingston DARM data from O4b to estimate squeezing parameters. Interactive fitting provided an intuitive and relatively quick way to infer and compare squeezing parameters over multiple data sets while MCMC fitting provided broader exploration of the squeezing parameter space, highlighting parameter degeneracy. A FINESSE model of the squeezed beam propagation path was also constructed and used to estimate mode matching to the OMC and the filter cavity as a function of strain gauge voltages on the ZM2,

ZM4, and ZM5 PSAMS. With the evolving nature of the LIGO detectors, having an up to date knowledge of squeezing loss sources is essential for guiding commissioning efforts and understanding the complex interaction between the squeezer and the interferometer.

Appendix A

The mode matching of two Gaussian beams with electric field E_1 and E_2 can be calculated using the overlap integral.

$$O = \frac{\left|\iint_{-\infty}^{\infty} E_1(x,y)^* E_2(x,y) dxdy\right|^2}{\iint_{-\infty}^{\infty} E_1(x,y)E_1^*(x,y)dxdy \iint_{-\infty}^{\infty} E_1(x,y)E_1^*(x,y)dxdy} \tag{6}$$

We will start by solving for the numerator using the definition of the electric field of a Gaussian beam.

$$E(x,y) = \frac{1}{\sqrt{q_x q_y}} \exp\left(-ik\frac{x^2}{2q_x}\right) \exp\left(-ik\frac{y^2}{2q_y}\right)$$

$$\begin{aligned}
&\left|\iint_{-\infty}^{\infty} \frac{1}{\sqrt{q_{1x}q_{1y}}} \exp\left(i\frac{k}{2}(\frac{x^2}{q_{1x}} + \frac{y^2}{q_{1y}})\right) \frac{1}{\sqrt{q_{2x}^* q_{2y}^*}} \exp\left(-i\frac{k}{2}(\frac{x^2}{q_{2x}^*} + \frac{y^2}{q_{2y}^*})\right) dxdy\right|^2 \\
&= \left|\frac{1}{\sqrt{q_{1x}q_{1y}q_{2x}^*q_{2y}^*}} \int_{-\infty}^{\infty} \exp\left(ix^2\frac{k}{2}(\frac{1}{q_{1x}} - \frac{1}{q_{2x}^*})\right) dx \int_{-\infty}^{\infty} \exp\left(iy^2\frac{k}{2}(\frac{1}{q_{1y}} - \frac{1}{q_{2y}^*})\right) dy\right|^2
\end{aligned}$$

Assuming that $\mathrm{Im}(q_{1x}) > \mathrm{Im}(q_{2x}^*)$ and $\mathrm{Im}(q_{1y}) > \mathrm{Im}(q_{2y}^*)$, we can employ the Gaussian integral solution [31].

$$\begin{aligned}
\left|\iint_{-\infty}^{\infty} E_1(x,y)E_2^*(x,y)\right|^2 dxdy &= \left|\frac{1}{\sqrt{q_{1x}q_{1y}q_{2x}^*q_{2y}^*}} \sqrt{\frac{\pi}{i\frac{k}{2}(\frac{1}{q_{1x}} - \frac{1}{q_{2x}^*})}} \sqrt{\frac{\pi}{i\frac{k}{2}(\frac{1}{q_{1y}} - \frac{1}{q_{2y}^*})}}\right|^2 \\
&= \left|\frac{2\pi}{k\sqrt{q_{1x}q_{1y}q_{2x}^*q_{2y}^*}} \sqrt{-\frac{q_{1x}q_{1y}q_{2x}^*q_{2y}^*}{(q_{1x} - q_{2x}^*)(q_{1y} - q_{2y}^*)}}\right|^2 \\
&= \left|\frac{\lambda}{\sqrt{-(q_{1x} - q_{2x}^*)(q_{1y} - q_{2y}^*)}}\right|^2
\end{aligned}$$

The denominator can be solved through similar computation.

$$\begin{aligned}
&\iint_{-\infty}^{\infty} E_1(x,y)E_1^*(x,y)dxdy \\
=&\frac{1}{\sqrt{q_{1y}q_{1y}^*q_{1x}q_{1x}^*}}\iint_{-\infty}^{\infty}\exp\left(-ix^2\frac{k}{2}(\frac{1}{q_{1x}}-\frac{1}{q_{1x}^*})\right)\exp\left(-iy^2\frac{k}{2}(\frac{1}{q_{1y}}-\frac{1}{q_{1y}^*})\right)dxdy \\
=&\frac{1}{|q_{1y}|\,|q_{1x}|}\sqrt{\frac{\pi}{i\frac{k}{2}(\frac{1}{q_{1x}}-\frac{1}{q_{1x}^*})}}\sqrt{\frac{\pi}{i\frac{k}{2}(\frac{1}{q_{1y}}-\frac{1}{q_{1y}^*})}} \\
=&\frac{2\pi\,|q_{1x}|\,|q_{1y}|}{k\,|q_{1y}|\,|q_{1x}|}\frac{1}{\sqrt{-(q_{1x}-q_{1x}^*)(q_{1y}+q_{1y}^*)}} \\
=&\frac{\lambda}{\sqrt{-(q_{1x}-q_{1x}^*)(q_{1y}-q_{1y}^*)}}
\end{aligned}$$

Repeating this for E_2 gives us,

$$\iint_{-\infty}^{\infty} E_2(x,y)E_2^*(x,y)dxdy = \frac{\lambda}{\sqrt{-(q_{2x}-q_{2x}^*)(q_{2y}-q_{2y}^*)}}$$

Substituting the solved integrals into eqn. 6 gives us

$$O = \frac{1}{\lambda^2}\left|\frac{\lambda}{\sqrt{-(q_{1x}-q_{2x}^*)(q_{1y}-q_{2y}^*)}}\right|^2\sqrt{(q_{1x}-q_{1x}^*)(q_{1y}-q_{1y}^*)(q_{2x}-q_{2x}^*)(q_{2y}-q_{2y}^*)}$$

Expanding out the absolute value and simplifying results in an expression for the mode matching of two Gaussian beams.

$$O = \sqrt{\frac{(q_{1x}-q_{1x}^*)(q_{1y}-q_{1y}^*)(q_{2x}-q_{2x}^*)(q_{2y}-q_{2y}^*)}{(q_{1x}-q_{2x}^*)(q_{1y}-q_{2y}^*)(q_{1x}^*-q_{2x})(q_{1y}^*-q_{2y})}}$$

Note that this solution is dependent on the convergence of the Gaussian integrals involved. This gives us a set of constraints on the complex beam parameters $q_{1x,y}$ and $q_{2x,y}$:

$$\begin{aligned}
\mathrm{Im}(q_{1x}) &> \mathrm{Im}(q_{2x}^*) \\
\mathrm{Im}(q_{1y}) &> \mathrm{Im}(q_{2y}^*) \\
\mathrm{Im}(q_{1x}) &> \mathrm{Im}(q_{1x}^*) \\
\mathrm{Im}(q_{2x}) &> \mathrm{Im}(q_{2x}^*)
\end{aligned}$$

These sets of conditions can only be satisfied if the beam parameter has a positive imaginary component. From eqn. 3, this physically corresponds to a positive Rayleigh range, which will be true for all complex beam parameters.

Appendix B

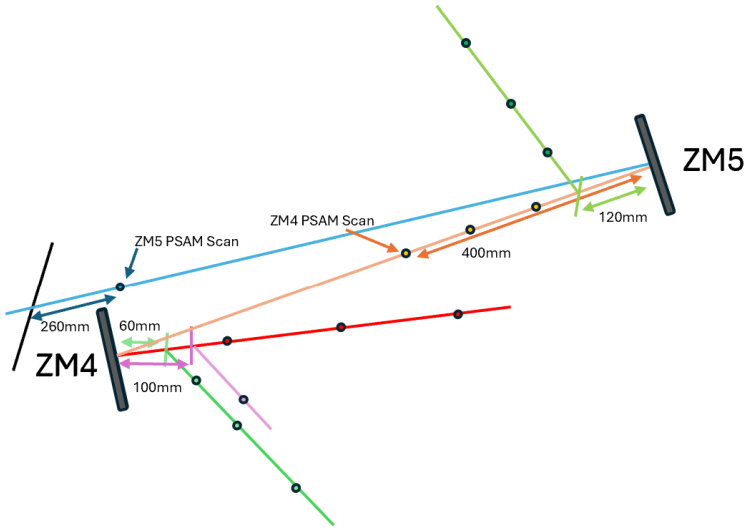

Figure 27: Diagram of the ZM4 and ZM5 beam profiling measurements. Flat diverting mirrors were used to measure the beam profile at distances beyond ZM4 and ZM5. ZM4 and ZM5 PZT voltages were swept while the beam size at each voltage was measured at the marked PSAM scan locations.

Acknowledgements

Many thanks to the National Science Foundation Research Experience for Undergraduates (NSF REU) program, the LIGO Laboratory Summer Undergraduate Research Fellowship program (NSF LIGO), the California Institute of Technology Student-Faculty Programs, and my research mentor, Begum Kabagöz.

References

[1] W. Jia, "Quantum noise modeling of ligo livingston detector in o4." T2300439.

[2] D. Ganapathy, "Interactive sqz analysis script." LH067565.

[3] W. Jia, "O4 gwinc quantum noise model - part ii: Calibrated shot noise." LLO69037.

[4] V. Frolov, "L1 arm power and test mass absorption in o4b." LLO71477.

[5] M. L. T. M. Yu, H. *et al.*, "Quantum correlations between light and the kilogram-mass mirrors of ligo.," *Nature*, vol. 583, p. 43–47, Sep 2020.

[6] W. Jia, "Quantum noise model inferred from 10/22/2023." LLO70078.

[7] D. A. Smith, "Interactive squeeze llo." Gitlab.

[8] B. Kabagöz, "Zm4 zm5 psam scans." LLO70218.

[9] https://ldas-jobs.ligo-la.caltech.edu/~detchar/summary/day/20240319/plots/L1-LOCKED_HOFT_M_SPECTROGRAM_SPECTROGRAM-1394841618-86400.png.

[10] J. Betzwieser, "Calibration sweeps during src offset changes, and calibration pushed." LLO70529.

[11] D. Foreman-Mackey, D. W. Hogg, D. Lang, and J. Goodman, "emcee: The mcmc hammer," *Publications of the Astronomical Society of the Pacific*, vol. 125, p. 306–312, Mar. 2013.

[12] N. Kijbunchoo, "Sqz loss/phase noise fitting." LHO49020.

[13] P. Kwee *et al.*, "Decoherence and degradation of squeezed states in quantum filter cavities," *Phys. Rev. D*, vol. 90, p. 062006, Sep 2014.

[14] M. Nakano, "Psam scans." LLO64645.

[15] B. Kabagoz, "Comment to: Running with lower input power over the weekend." LLO72249.

[16] B. Kabagoz, "Psam scan." LLO72113.

[17] M. Nakano, "Psams scan result(llo)." T2200151.

[18] B. Kabagoz, "Zm4 zm5 psam scans." LLO70218.

[19] B. Kabagoz, "Sqz alignment study after co2 is back." LLO72441.

[20] B. Kabagoz, "Ham 7 distances for llo sqz finesse model." LLO71618.

[21] A. Mullavey, "Ham7 - zm2 psam optimization and beam profiling near zm4/zm5." LLO59820.

[22] L. B. L. McCuller, S. Biscans, "Frequency dependent squeezing final optical layout." T1900649-v8.

[23] M. Nakano, "Omc mode scan for sqz beam), note = llo59841."

[24] A. Mullavey, "Recent sqz level summary." LLO71584.

[25] M. Nakano, "5.4db squeezing." LLO63493.

[26] M. Nakano, "Fc alignment finalization." LLO6309.

[27] "Ligo commissioning modeling." Gitlab.

[28] M. Nakano, "Continue to setup a path and a part of h path." LLO55863.

[29] M. Nakano, "B path alignment and modematching." LLO56353.

[30] A. Mullavey. Private correspondence.

[31] R. Littlejohn, "Gaussian Integrals."